Satellite geodetic imaging reveals internal deformation of western Tibet

H. Wang[1,2] and T. J. Wright[2]

[1] It is often assumed that the majority of the interseismic strain accumulates around the major mapped geological block boundaries. However, numerous recent earthquakes in the continents have occurred on faults that were previously unidentified. Existing deformation data from Tibet are insufficiently dense to map the distribution of interseismic strain. Here we combine 265 interferograms formed from 166 radar images with GPS data to constrain a high-resolution velocity field covering ~200,000 km^2 of western Tibet. We confirm that the slip rate of the Karakoram Fault is low (<6 mm/yr), but show that areas of focused strain do not coincide with the major fault structures. Some of this strain is due to postseismic relaxation after a M_w 6.8 earthquake that occurred in 1996 on a structure that is difficult to identify in satellite imagery. Models of seismic hazard that rely on imperfect knowledge of the boundaries of crustal blocks can therefore underestimate hazard from unknown faults. **Citation:** Wang, H., and T. J. Wright (2012), Satellite geodetic imaging reveals internal deformation of western Tibet, *Geophys. Res. Lett.*, *39*, L07303, doi:10.1029/2012GL051222.

1. Introduction

[2] Earthquakes in continental interiors have killed more than a million people in the past century [*England and Jackson*, 2011]. Despite improved mapping of the location of active faults [*Jackson*, 2001], earthquakes, such as the Darfield/Christchurch events of 2010/2011, continue to occur in unexpected locations, even in well-studied areas like New Zealand [*England and Jackson*, 2011]. Observations of crustal deformation from satellite geodesy can be used to map the accumulation of tectonic strain in the interseismic period. A key question is how much of this strain can be attributed to the major faults of a region. The ongoing collision of India with Asia, which has created the Himalayas and Tibetan plateau, provides a natural laboratory in which this question can be addressed.

[3] Western Tibet is the narrowest part of the Tibetan plateau, squeezed between India and the rigid Tarim Basin. Two >1000-km-long strike-slip faults lie within this region: the NW-SE-aligned right-lateral Karakoram Fault (KF) in the south and the western end of the E-W-aligned left-lateral Altyn Tagh Fault (ATF), also known as the Karakash fault, in the north. The Longmu-Gozha Co (LGC) left-lateral strike-slip fault intersects both ATF and KF, separating the Tianshuihai terrane to the northwest from the Tibetan plateau to the southeast (Figure 1). These structures are clearly visible as major features in satellite imagery and topographic data − they have been assumed to dominate the deformation within the region [e.g., *Meade*, 2007; *Thatcher*, 2007].

[4] Existing observations of crustal deformation in Tibet are largely derived from GPS [e.g., *Gan et al.*, 2007]. The enormity of the plateau and the lack of easy access routes have resulted in large gaps in GPS coverage, particularly in central and western Tibet. Interferometric Synthetic Aperture Radar (InSAR) offers an independent means of measuring present-day crustal deformation. By differencing the phase observations from multiple radar images, line-of-sight (LOS) interseismic deformation can be measured with a spatial resolution of a few tens of meters and accuracy comparable to GPS [e.g., *Wright et al.*, 2001, 2004a; *Wang et al.*, 2009]. Western Tibet is sparsely covered by GPS, but well suited to InSAR observations because of a large radar data archive, fairly good coherence and low atmospheric delay errors [*Wright et al.*, 2004a]. Data from Sentinel-1, due to be launched in 2013, will enable high-resolution velocity fields to be built for entire continents using the methods presented here.

2. InSAR Data Analysis

[5] Using the JPL/Caltech ROI_PAC software [*Rosen et al.*, 2004], we produce 265 interferograms with radar images acquired by the ERS-1/2 and Envisat satellites between 1992 and 2010 on six tracks. Most interferograms have perpendicular baselines smaller than 200 m and are formed from images acquired during the same season (Figure S1 in the auxiliary material).[1] Topographic phase is removed using the 3-arc-second SRTM DEM [*Farr et al.*, 2007]. Some isolated patches have to be unwrapped manually by setting bridges due to loss of coherence. The interferograms have been checked to exclude phase unwrapping errors using a phase closure technique based on minimum spanning tree [*Kruskal*, 1956] and Dijkstra algorithms [*Dijkstra*, 1959]. For track 248, we did not use coseismic interferograms covering the Yutian earthquake, and masked ± 170 km around its epicenter for postseismic pairs.

[6] A network-based approach is then used to mitigate orbital and linear topographically-correlated atmospheric delay errors in the interferograms, and finally estimate the interseismic deformation rates and the associated uncertainties for each track (Figures 2 and S2) [*Biggs et al.*, 2007; *Wang et al.*, 2009]. Many interferograms cannot be unwrapped across the ATF due to loss of coherence. We

---

[1]Department of Surveying Engineering, Guangdong University of Technology, Guangzhou, China.
[2]COMET+, School of Earth and Environment, University of Leeds, Leeds, UK.
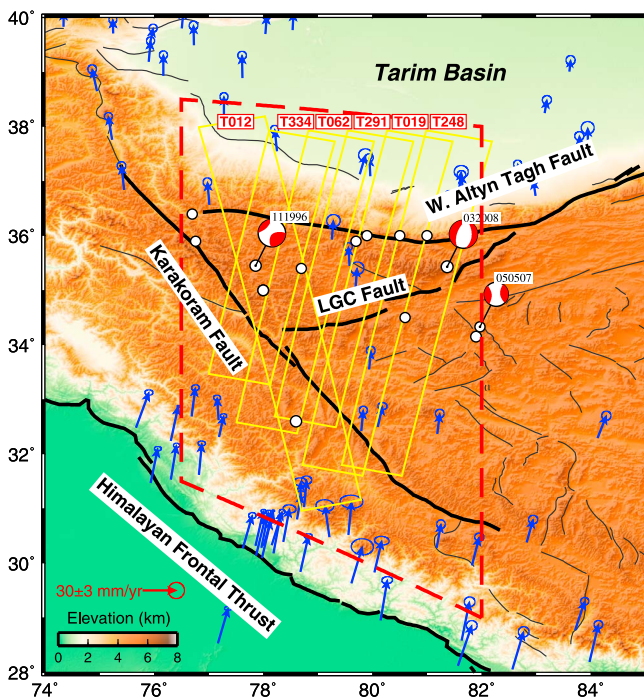

Figure 1. Topographic and tectonic map of western Tibet. The red dashed box indicates the region of our velocity field in Figure 3. The thick black lines indicate the major faults in western Tibet [*Taylor and Yin*, 2009]. The yellow rectangles delimit the extents of ERS and Envisat radar imagery on one ascending (012) and five descending tracks (334/062/291/019/248). The blue arrows show GPS velocities with respect to stable Eurasia [*Gan et al.*, 2007]. The white circles are historical *M* > 6 earthquakes since 1900 from the China Earthquake Administration [*DEMP*, 1999] and the Harvard CMT catalogue. Red-white spheres are the focal mechanisms of the *M* > 6 earthquakes occurring since 1990.

therefore unwrap the interferograms for the north and south side of the ATF individually and generate two unwrapped images for each interferogram. Thus two rate maps are made separated by the ATF for each track. The velocity field method described in the following section does not require full coverage of the study area and can deal with multiple rate maps, so that the splitting of the interferograms for phase unwrapping does not contaminate the estimated velocity field and the resultant conclusions.

3. Velocity Field Inversion

[7] We adapt velocity field methods previously applied to GPS data [*England and Molnar*, 2005] to combine the twelve InSAR rate maps from six tracks, with different line-of-sight viewing geometries, with the available GPS data. This allows us to form a velocity field in the GPS reference frame with higher spatial resolution than is available from the sparse GPS data alone. Following *England and Molnar* [2005], we divide western Tibet into a triangular mesh, and assume the velocity varies linearly with latitude and longitude within each triangle. Therefore, the geodetic observations within each triangle are related to the velocities of its vertices by an interpolation function.

[8] Although the resolution of the velocity field is significantly lower than that of the original InSAR data (the edges of our triangles are typically ∼ 20 km) this has the benefit of filtering out short-wavelength noise, unrelated to tectonic motions. An additional advantage of the method is that it can provide velocities (and their uncertainties) even in areas of InSAR incoherence.

[9] Given GPS velocities $\mathbf{d}_{gps}$ and InSAR displacement rates $\mathbf{d}_{sar}$, the system of equations can be written as

$$\begin{bmatrix} \mathbf{G}_{sar} & \mathbf{G}_{orb} & \mathbf{G}_{atm} \\ \mathbf{G}_{gps} & 0 & 0 \\ \kappa^2\nabla^2 & 0 & 0 \end{bmatrix} \begin{bmatrix} \mathbf{m}_{vel} \\ \mathbf{m}_{orb} \\ \mathbf{m}_{atm} \end{bmatrix} = \begin{bmatrix} \mathbf{d}_{sar} \\ \mathbf{d}_{gps} \\ 0 \end{bmatrix}, \quad (1)$$
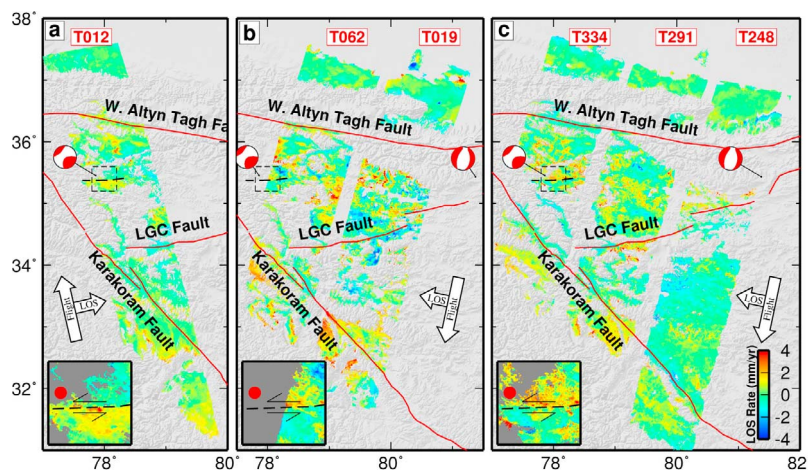

Figure 2. InSAR rate maps showing LOS displacement rates, after correction for orbital and atmospheric delay errors. (a) Ascending track 012, (b) descending tracks 062 and 019, (c) descending tracks 334, 291 and 248. Positive values indicate motion away from satellite. Gray pixels within the tracks mean loss of coherence or high uncertainty of deformation rate (>1mm/yr). The white arrows show radar LOS and flight directions. Insets show details of the rate maps around the 1996 *M*_w 6.8 earthquake, whose surface rupture from a coseismic interferogram (Figure S9) is shown as a black dashed line.
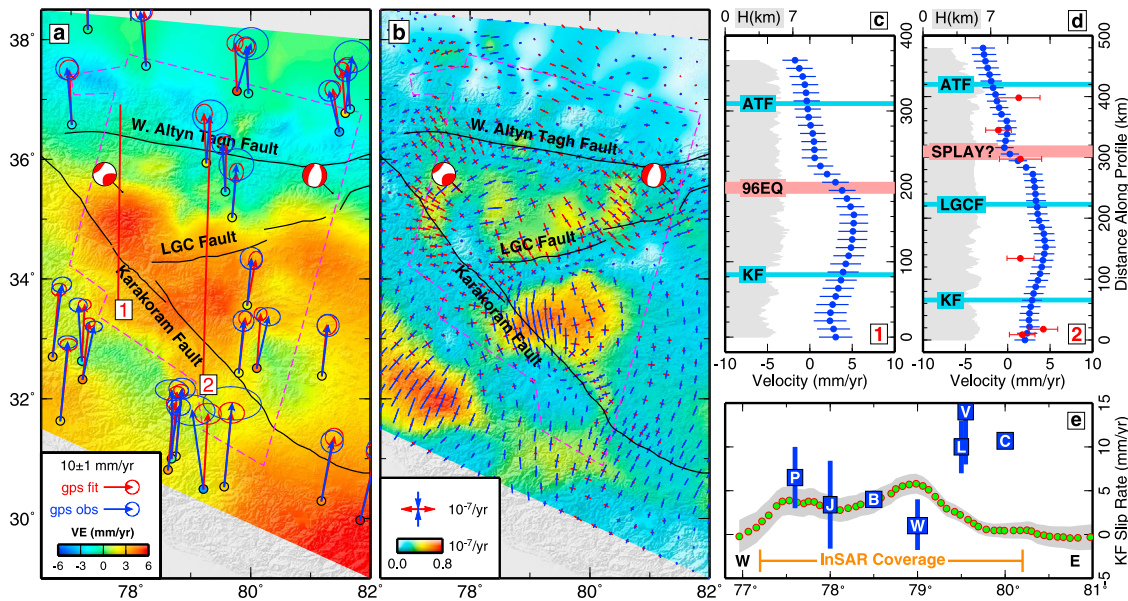
Figure 3. Velocity and strain rate field derived from GPS and InSAR data. (a) East components of crustal velocity field in western Tibet. Colored circles denote east components of the observed GPS velocities. Blue and red arrows show the observed and fitted horizontal GPS velocities respectively. The dashed polygon indicates InSAR coverage. (b) The background color pattern show the magnitude of second invariant of strain rate tensor derived from the velocities on the vertices. Red and blue bars indicate extensional and compressional principal strain rates respectively. (c, d) Blue circles indicate velocities perpendicular to the profiles in Figure 3a (eastward positive), and the red show that from six nearest GPS sites along profile 2. Error bars denote 1σ uncertainties. Cyan bars indicate major fault zones, and the red indicate locations of strain associated with postseismic deformation and a splay of the LGC fault. The grey bands show elevation along the profiles. (e) Green circles denote slip rates along the KF with 1σ error bounds shown in grey band. The horizontal bar indicates the portion of the fault covered by InSAR data. Blue bars are slip rates compiled from the previous studies, including W, *Wright et al.* [2004a]; L, *Lacassin et al.* [2004]; C, *Chevalier et al.* [2005]; V, *Valli et al.* [2008]; B, *Brown et al.* [2002]; J, *Jade et al.* [2004]; P, *Phillips and Searle* [2007].

where $\mathbf{G}_{sar}$ is the design matrix for InSAR rate maps composed of interpolation kernel and local LOS unit vectors; $\mathbf{G}_{orb}$ and $\mathbf{G}_{atm}$ are matrices for InSAR orbital and topographically-correlated atmospheric delay correction models ($\mathbf{m}_{orb}$ and $\mathbf{m}_{atm}$); $\mathbf{G}_{gps}$ is the design matrix composed of the interpolation kernel for GPS velocities; $\mathbf{m}_{vel}$ is the unknown velocities of the triangular vertices. We use smoothing constraints to remove short-wavelength features in the interferograms that we assume have non-tectonic origin. ∇^2 is the Laplacian smoothing operator approximated by a scale-dependent umbrella operator [*Desbrun et al.*, 1999], and the factor κ^2 determines the weight of smoothing. A quadratic model $\mathbf{G}_{orb}$ is used here to fit orbital and long wavelength atmospheric delay errors (examples in Figure S3).

[10] The system of equations can be solved to yield the velocity field using a biconjugate gradients method with a full covariance matrix, which is formed by the formal uncertainties of GPS data and the full covariance matrix of InSAR data modeled using an exponential function [*Parsons et al.*, 2006]. Because of the sparse distribution of GPS sites, we find that increasing the weight of GPS with respect to InSAR does not change our results significantly. With the above velocity field model, we can also get a continuous velocity field by interpolation of the velocities of the vertices. Finally, we calculate the strain rate at each vertex with the velocity field model using spherical approximation equations [*Savage et al.*, 2001].

[11] The best-fit velocity field depends on the smoothing factor − we select a value that has low misfit but is not too rough by using a trade-off curve between weighted misfit and solution roughness. Varying the smoothing factor changes the magnitude of the inverted velocities and strains but does not alter their spatial pattern (Figures S4 and S5). The under-smoothed solution (Figure S5a–S5c) is likely excluded as the unusual large and rough strain rates are mostly due to spatial variation of noise. We note that the strain is higher away from the block-bounding faults even in the over-smoothed solution (Figures S5g–S5i).

[12] Because radar satellites available for interferometry are in near-polar orbits and are side-looking, interferograms are mostly sensitive to vertical and east-west motion, and only weakly sensitive to north-south velocities [*Wright et al.*, 2004b]. Furthermore, only horizontal GPS velocities are available in Tibet. For our preferred solution (Figure 3), we therefore chose to assume that vertical velocities are negligible. Preliminary findings from unpublished vertical GPS data suggest that this assumption is reasonable for the plateau interior, although systematic uplift of up to 8 mm/yr may occur near the Himalayas [*Freymueller et al.*, 2010]. We carried out an additional test of this assumption by inverting for east-west and vertical velocities in the region where we have overlapping ascending and descending interferograms; north-south velocities were prescribed from GPS alone. The relative vertical velocities in the region bounded by the KF, ATF and LGCF were less than 2 mm/yr

(Figure S6). Importantly, the east-west velocities were nearly identical (RMS difference of 0.8 mm/yr) to those found when inverting for only horizontal velocities (Figures 3 and S6d). Similarly, the east-west velocities do not change significantly whether we invert for north-south velocities using all the geodetic data, or use only GPS for the north-south component (Figures 3 and S7a). Conversely, the accuracy of north-south velocities is not significantly improved by the addition of InSAR data (Figure S8). The final root-mean-square misfit is 1.8 mm/yr for GPS data and 0.7 mm/yr for the InSAR rate maps, which are comparable to the uncertainties of GPS and InSAR deformation rates respectively. Uncertainties in the velocities increase with distance from GPS stations, but in the region of InSAR coverage are typically 1–1.5 mm/yr for east-west velocities and 2–2.5 mm/yr for the north-south component (Figure S8).

4. Discussion

[13] As expected, the velocity field fitted with InSAR and GPS data shows a more detailed deformation field than that fitted with GPS data alone (Figures 3 and S7d–S7f), particularly within the Tianshuihai terrane enclosed by the Altyn Tagh, LGC and Karakoram faults. In particular, profiles through the velocity field reveal two zones of focused left-lateral shear away from the major faults (Figures 3c and 3d). The left-lateral strain in profile 1 (Figure 3c) is coincident with the location of a M_w 6.8 strike-slip earthquake that occurred in 1996. A coseismic interferogram for this earthquake shows that it involved left-lateral slip on an east-west plane, and allows us to map its surface rupture (Figure S9). Postseismic interferograms for the 1997 Manyi and 2001 Kokoxili earthquakes [Ryder et al., 2007, 2011], both also east-west, left-lateral strike-slip events in Tibet, show negative range changes on the north side of the rupture relative to the south side in ascending interferograms, and vice versa in descending data. We observe such range changes in all three independent InSAR rate maps that cover the surface rupture of the 1996 earthquake (insets in Figure 2). The signal has a peak-to-peak amplitude of ∼5 mm/yr over ∼50 km, which is comparable to the predictions of a visco-elastic postseismic model using the viscosity structure determined for the 1997 Manyi earthquake (Figure S10) [Ryder et al., 2007, 2011]. We are therefore confident that this high strain zone represents post-seismic deformation from the 1996 earthquake. The fault that ruptured during this earthquake does not appear on any published fault maps and lacks a significant geomorphological expression (Figure S9).

[14] Another strongly localized gradient phenomena is evident in Figure 3d, implying ∼4 mm/yr left-lateral motion on a structure north of the LGC fault, comparable to the rates estimated using InSAR data in central Tibet [Taylor and Peltzer, 2006]. Our result here, derived primarily from Envisat data acquired between 2003 and 2010, is consistent with that observed in a stack of five interferograms with ERS-1/2 data from the 1990s [Wright et al., 2004a] and is also visible as an offset in the GPS data (Figure 3d). We suggest that this strain is due to an un-mapped splay of the LGC fault. It is unclear why deformation here is larger than is observed on the mapped faults of the region.

[15] The slip rate of the KF has been particularly controversial in recent years, with rates as high as 10–30 mm/yr estimated in some geological studies [e.g., Peltzer and Tapponnier, 1988; Lacassin et al., 2004; Chevalier et al., 2005; Valli et al., 2008], contrasting with significantly lower estimates from geodetic and other geological investigations [e.g., Brown et al., 2002; Jade et al., 2004; Wright et al., 2004a; Phillips and Searle, 2007]. Our InSAR rate maps cover most of the KF with both descending and ascending data, so our velocity field is very well constrained around the fault. By fitting fault parallel velocity across the KF with an elastic dislocation model [Savage and Burford, 1973], we have estimated the variation in slip rate along the fault, assuming all the strain is accommodated by motion on the KF (Figure 3e). We find that the right-lateral slip rate of the KF varies from 0 to 6 mm/yr with an uncertainty of 1–2 mm/yr. The highest slip rate is in the central portion near the intersection with the LGC fault. The results rule out present-day slip rates of 10 mm/yr or higher.

[16] The strain rate field derived from the velocity field (Figure 3b) identifies several areas of focused strain, particularly within the Tianshuihai terrane, where at least three M>6 earthquakes have occurred since 1900, comparable to the number of earthquakes thought to have occurred on the ATF (5), KF (1) and LGC (2) faults according to the China Earthquake Administration [Division of Earthquake Monitoring Prediction (DEMP), 1999] and the Harvard Centroid Moment Tensor (CMT) catalogues (Figure 1). The focused strain zones that we observe are not obviously associated with the major faults of the region. A common strategy for modelling deformation of the continents is to divide a region into a number of rigid crustal blocks, each bounded by fault zones where all the strain and earthquakes occur [e.g., Meade, 2007; Thatcher, 2007]. These block models provide predictions for the slip rates on the block-bounding faults, and therefore inform seismic hazard assessments. Although we could clearly construct such a model that would fit our new velocities, by including new block boundaries in areas where we have identified strain, the size of these blocks would be relatively small compared to the lithospheric thickness. Similar results have been found in the Aegean [Nyst and Thatcher, 2004; Floyd et al., 2010] and Basin and Range [Hammond et al., 2011]. It is unlikely that such blocks would dominate the dynamics of the region. Given our imperfect knowledge of the location of seismogenic faults in the continents [England and Jackson, 2011], we argue that it is dangerous to ascribe significant hazard only to those faults assumed to be block boundaries from geological data alone.

[17] Our results show that dense geodetic data are required to fully characterize the instantaneous velocity field of a continental region, and that the velocities may not conform to expectations based on geological interpretations. The identification here of high strain zones away from the major faults of western Tibet implies that instantaneous crustal velocities are in turn biased by non-steady phenomena including postseismic relaxation, which can persist for decades [Gourmelen and Amelung, 2005]. A new generation of seismic hazard models should be developed that incorporate time-varying strain measurements now available from satellite geodesy.

References

Biggs, J., et al. (2007), Multi-interferogram method for measuring interseismic deformation: Denali Fault, Alaska, *Geophys. J. Int.*, *170*, 1165–1179.

Brown, E. T., R. Bendick, D. L. Bourlès, V. Gaur, P. Molnar, G. M. Raisbeck, and F. Yiou (2002), Slip rates of the Karakorum fault, Ladakh, India, determined using cosmic ray exposure dating of debris flows and moraines, *J. Geophys. Res.*, *107*(B9), 2192, doi:10.1029/2000JB000100.

Chevalier, M.-L., et al. (2005), Slip-rate measurements on the Karakorum fault may imply secular variations in fault motion, *Science*, *307*, 411–414.

Desbrun, M., M. Meyer, P. Schroder, and A. H. Barr (1999), Implicit fairing of irregular meshes using diffusion and curvature flow, *SIGGRAPH*, *99*, 317–324.

Dijkstra, E. W. (1959), A note on two problems in connexion with graphs, *Numer. Math.*, *1*, 269–271.

Division of Earthquake Monitoring and Prediction (DEMP) (1999), *Catalogue of Chinese Modern Earthquakes* [in Chinese], Sci. and Technol. Press, Beijing.

England, P., and J. Jackson (2011), Uncharted seismic risk, *Nat. Geosci.*, *4*, 348–349.

England, P., and P. Molnar (2005), Late Quaternary to decadal velocity fields in Asia, *J. Geophys. Res.*, *110*, B12401, doi:10.1029/2004JB003541.

Farr, T. G., et al. (2007), The Shuttle Radar Topography Mission, *Rev. Geophys.*, *45*, RG2004, doi:10.1029/2005RG000183.

Floyd, M. A., et al. (2010), A new velocity field for Greece: Implications for the kinematics and dynamics of the Aegean, *J. Geophys. Res.*, *115*, B10403, doi:10.1029/2009JB007040.

Freymueller, J. T., et al. (2010), How rapidly is the Tibetan Plateau rising, and what fraction of that is tectonic?, Abstract T41D-03 presented at 2010 Fall Meeting, AGU, San Francisco, Calif., 13–17 Dec.

Gan, W., P. Zhang, Z.-K. Shen, Z. Niu, M. Wang, Y. Wan, D. Zhou, and J. Cheng (2007), Present-day crustal motion within the Tibetan Plateau inferred from GPS measurements, *J. Geophys. Res.*, *112*, B08416, doi:10.1029/2005JB004120.

Gourmelen, N., and F. Amelung (2005), Postseismic mantle relaxation in the central Nevada seismic belt, *Science*, *310*, 1473–1476.

Hammond, W. C., G. Blewitt, and C. Kreemer (2011), Block modeling of crustal deformation of the northern Walker Lane and Basin and Range from GPS velocities, *J. Geophys. Res.*, *116*, B04402, doi:10.1029/2010JB007817.

Jackson, J. (2001), Living with earthquakes: Know your faults, *J. Earthquake Eng.*, *5*, 5–123.

Jade, S., et al. (2004), GPS measurements from the Ladakh Himalaya, India: Preliminary tests of plate-like or continuous deformation in Tibet, *Geol. Soc. Am. Bull.*, *116*(11–12), 1385–1391.

Kruskal, J. B. (1956), On the shortest spanning subtree of a graph and the traveling salesman problem, *Proc. Am. Math. Soc.*, *7*, 48–50.

Lacassin, R., et al. (2004), Large-scale geometry, offset and kinematic evolution of the Karakorum fault, Tibet, *Earth Planet. Sci. Lett.*, *219*(3–4), 255–269.

Meade, B. J. (2007), Present-day kinematics at the India-Asia collision zone, *Geology*, *35*(1), 81–84.

Nyst, M., and W. Thatcher (2004), New constraints on the active tectonic deformation of the Aegean, *J. Geophys. Res.*, *109*, B11406, doi:10.1029/2003JB002830.

Parsons, B., et al. (2006), The 1994 Sefidabeh (eastern Iran) earthquake revisited: New evidence from satellite radar interferometry and carbonate dating about the growth of an active fold above a blind thrust fault, *Geophys. J. Int.*, *164*, 202–217.

Peltzer, G., and P. Tapponnier (1988), Formation and evolution of strike-slip faults, rifts and basins during the Indian-Asia collision: An experimental approach, *J. Geophys. Res.*, *93*(B12), 15,085–15,117.

Phillips, R. J., and M. P. Searle (2007), Macrostructural and microstructural architecture of the Karakoram fault: Relationship between magmatism and strike-slip faulting, *Tectonics*, *26*, TC3017, doi:10.1029/2006TC001946.

Rosen, P. A., S. Hensley, G. Peltzer, and M. Simons (2004), Updated repeat orbit interferometry package released, *Eos Trans. AGU*, *85*(5), 47, doi:10.1029/2004EO050004.

Ryder, I., B. Parsons, T. J. Wright, and G. J. Funning (2007), Post-seismic motion modelling, *Geophys. J. Int.*, *169*(3), 1009–1027.

Ryder, I., R. Burgmann, and F. Pollitz (2011), Lower crustal relaxation beneath the Tibetan Plateau and Qaidam Basin following the 2001 Kokoxili earthquake, *Geophys. J. Int.*, *187*(2), 613–630.

Savage, J. C., and R. O. Burford (1973), Geodetic determination of relative plate motion in central California, *J. Geophys. Res.*, *78*, 832–845.

Savage, J. C., W. Gan, and J. L. Svarc (2001), Strain accumulation and rotation in the Eastern California Shear Zone, *J. Geophys. Res.*, *106*(10), 21,995–22,007.

Taylor, M., and G. Peltzer (2006), Current slip rates on conjugate strike-slip faults in central Tibet using synthetic aperture radar interferometry, *J. Geophys. Res.*, *111*, B12402, doi:10.1029/2005JB004014.

Taylor, M., and A. Yin (2009), Active structures of the Himalayan-Tibetan orogen and their relationships to earthquake distribution, contemporary strain field and cenozoic volcanism, *Geosphere*, *5*(3), 199–214.

Thatcher, W. (2007), Microplate model for the present-day deformation of Tibet, *J. Geophys. Res.*, *112*, B01401, doi:10.1029/2005JB004244.

Valli, F., et al. (2008), New U-Th/Pb constraints on timing of shearing and long-term slip-rate on the Karakorum fault, *Tectonics*, *27*, TC5007, doi:10.1029/2007TC002184.

Wang, H., T. J. Wright, and J. Biggs (2009), Interseismic slip rate of the northwestern Xianshuihe fault from InSAR data, *Geophys. Res. Lett.*, *36*, L03302, doi:10.1029/2008GL036560.

Wright, T., B. Parsons, and E. Fielding (2001), Measurement of interseismic strain accumulation across the North Anatolian Fault by satellite radar interferometry, *Geophys. Res. Lett.*, *28*(10), 2117–2120.

Wright, T. J., et al. (2004a), InSAR observations of low slip rates on the major faults of western Tibet, *Science*, *305*, 236–239.

Wright, T. J., B. E. Parsons, and Z. Lu (2004b), Toward mapping surface deformation in three dimensions using InSAR, *Geophys. Res. Lett.*, *31*, L01607, doi:10.1029/2003GL018827.

H. Wang, Department of Surveying Engineering, Guangdong University of Technology, Guangzhou 510006, China. (ehwang@163.com)

T. J. Wright, COMET+, School of Earth and Environment, University of Leeds, Leeds LS2 9JT, UK. (t.wright@see.leeds.ac.uk)